ELSEVIER

Contents lists available at ScienceDirect

## **Chemical Physics Impact**

journal homepage: www.sciencedirect.com/journal/chemical-physics-impact





# Highly photoactive rGO-MnO<sub>2</sub>/CuO nanocomposite photocatalyst for the removal of metanil yellow dye and bacterial resistance against *Pseudomonas Aeruginosa*

A. Ceril Jeoffrey a,b, S. Jothi Ramalingam, K. Murugaiah, A.R. Balu c,

- <sup>a</sup> Chemistry Department, AVVM Sri Pushpam College (Affiliated to Bharathidasan University, Tiruchirappalli), Poondi, Tamilnadu, India
- <sup>b</sup> Chemistry Department, St. Joseph's College, Tiruchirappalli, Tamilnadu, India
- <sup>c</sup> Physics Department, AVVM Sri Pushpam College, Poondi, Tamilnadu, India

#### ARTICLE INFO

#### Keywords: Chemical precipitation nanocomposite energy band gap photodegradation reduced graphene oxide

#### ABSTRACT

The superior photocatalytic, biological, and electrochemical properties of metal oxide nanocomposites have made them an important part of contemporary nanotechnology research. Nanocomposite involving MnO2 and CuO has been widely utilized for catalytic and electrochemical applications. However, the different oxidation states of MnO2 and lower band gap of CuO limits the efficiency of the devices involving the composite of these two semiconductors. As a result, reduced graphene oxide (rGO) is integrated into the MnO<sub>2</sub>/CuO matrix. rGO-MnO<sub>2</sub>/CuO and MnO<sub>2</sub>/CuO nanocomposites (NCs) were synthesized using one-pot green synthesis and chemical precipitation respectively. rGO decorated MnO2/CuO NC was green synthesized from graphene oxide using Alternanthera sessilis leaf extract. XRD detected peaks related to orthorhombic structured MnO2 and monoclinic structured CuO for both the composites. Star shaped nanostructures are observed for rGO incorporated MnO<sub>2</sub>/ CuO nanocomposite. MC and rMC composites have band gaps of 2.16 and 2.04 eV, respectively. FTIR spectrum showed the characteristic peaks for MnO<sub>2</sub> and CuO in the rGO-MnO<sub>2</sub>/ CuO composite. Raman active  $A_{\sigma}$  and  $B_{\sigma}$ CuO modes occur at 270 and 450 cm<sup>-1</sup> and Mn-O symmetric vibrations at 590 and 540 cm<sup>-1</sup>. The incorporation of rGO into the MnO2/CuO composite increased its photocatalytic activity from 87 % to 96 % against the degradation of metanil yellow dye by increasing its electron conductivity, adsorption capacity, and light absorption capacity. The MnO2/CuO nanocomposite with rGO demonstrated enhanced antibacterial activity, with a zone of inhibition of 24 mm compared to 13 mm for the control and 18 mm for the MnO<sub>2</sub>/CuO composite.

#### 1. Introduction

The surrounding ecosystem and human health are seriously threatened by the growing amount of waste water carrying dangerous organic contaminants from diverse enterprises [1]. Water pollution is exacerbated by dyes, which are poisonous and often produced in industrial settings. The removal of organic contaminants from water has been attempted using advanced oxidation processes (AOPs). Photocatalysis, which may be carried out with just a catalyst and light, is the most efficient AOP for cleaning pollutants out of water [2]. Metal oxide semiconductors have become popular for environmental pollution cleanup due to their photosensitivity and non-toxicity [3]. With the application of photocatalytic semiconductors, water and air can be purified in a scientifically sound manner. Furthermore, it is used for the

regulation of odor, the production of hydrogen, and the inactivation of bacteria and cancer cells. Metal oxide semiconductors like ZnO [4], TiO<sub>2</sub> [5], NiO [6], SnO<sub>2</sub> [7], etc. are often used in catalytic applications. In addition to these wide band oxides, lower band gap oxides such as CdO [8], Cu<sub>2</sub>O [9], MnO [10], BiVO<sub>4</sub> [11] are also used for catalytic applications. However, using a single semiconductor has problems such as sluggish photocatalyst deactivation, low visible light harvest, poor selective adsorption, and quick electron-hole pair recombination. Combining two distinct types of metal oxides to produce a composite material that enables the effective mutual movement of charge carriers from one semiconductor to another is the strategy that has proven to be the most successful in meeting the requirements of these problems. Two semiconductors MnO<sub>2</sub> and CuO were coupled to form composite in this work.

E-mail address: arbalu757@gmail.com (A.R. Balu).

<sup>\*</sup> Corresponding author:

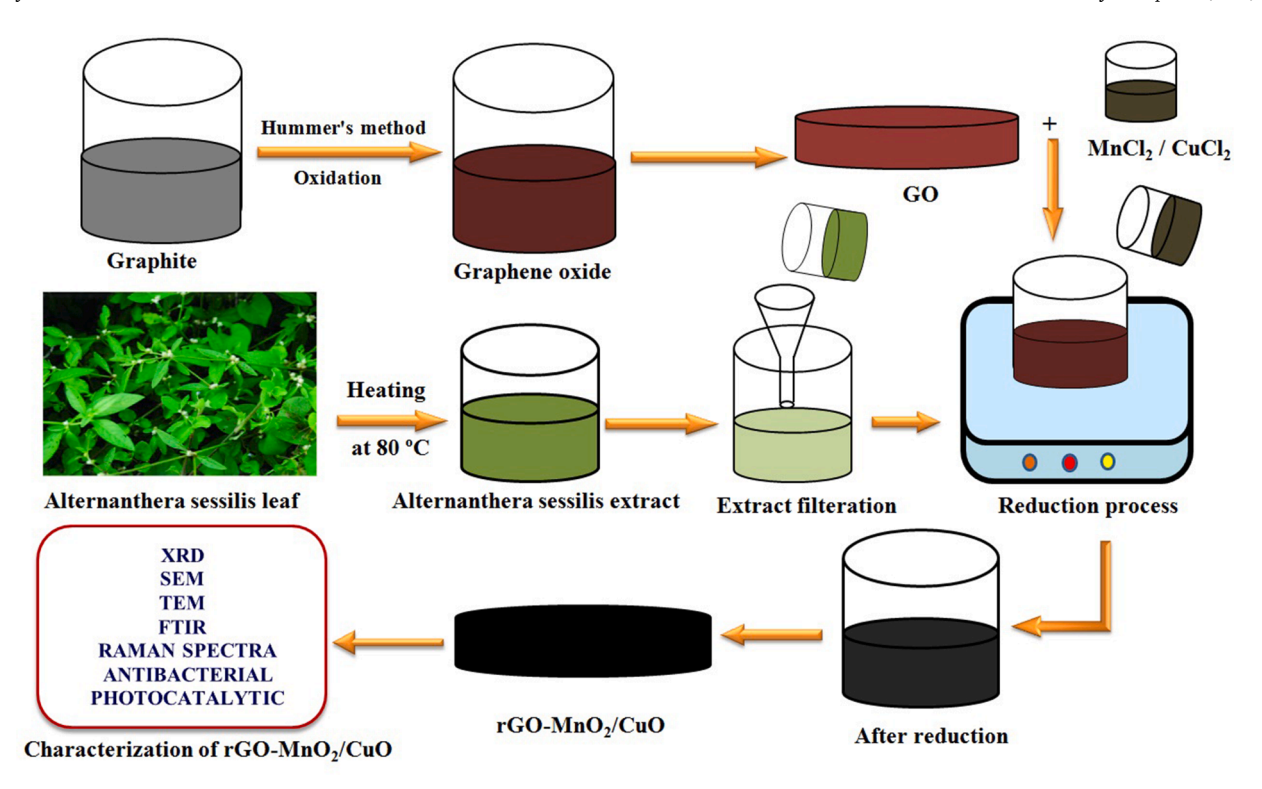
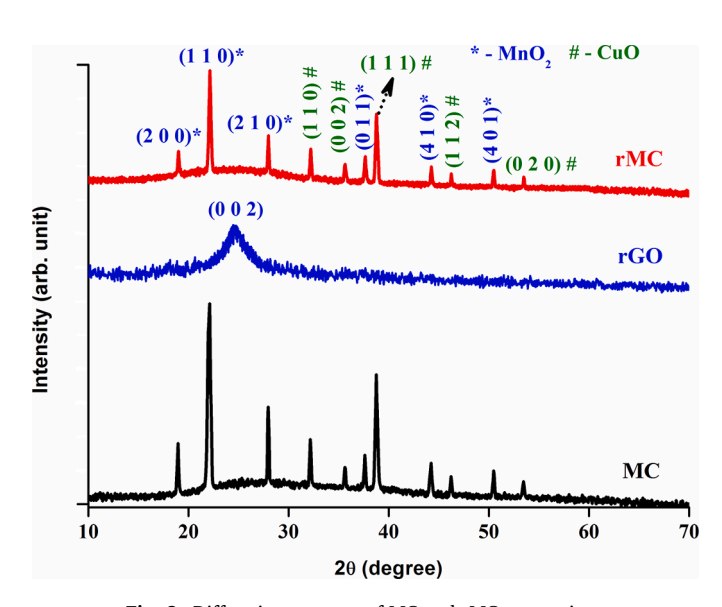


Fig. 1. Synthesizing procedure of rMC composite



 $\textbf{Fig. 2.} \ \ \textbf{Diffraction patterns of MC and rMC composites}$ 

The stable oxide manganese dioxide (MnO<sub>2</sub>) has a high surface area, strong chemical resistance, and catalytic behavior [12]. MnO<sub>2</sub> is a possible pseudo-capacitive oxide with a capacitance of up to 1370 F/g [13]. MnO<sub>2</sub> nanostructures suited for catalytic activities have been controlled synthesized by Sun et al. [14]. Catalytic combustion of toluene using hierarchical MnO<sub>2</sub> via  $\rm H_2O_2$  selectively reducing KMnO<sub>4</sub> has been reported by Chen et al. [15]. Two dimensional MnO<sub>2</sub> nanosheets has been reported to promote ultra-sensitive pH-triggered theranostics of cancer by Chen et al. [16]. MnO<sub>2</sub> NPs with biomedical properties has been synthesized by Chen et al. [17]. However, poor electron conductivity and instability are drawbacks that limit MnO<sub>2</sub>'s use in pseudo-capacitors and catalytic applications.

Among the applications of CuO, a p-type semiconductor with a

narrow band gap, are high temperature superconductors, photovoltaic materials, field emission, and catalysis [18]. The anticancer, antibacterial, and antioxidant properties of CuO nanoparticles make them an attractive biomedical material [19]. Green CuO nanoparticles possess antibacterial activity against urinary tract pathogens [20]. Singh et al. [21] bio-synthesised CuO NPs suitable for electrochemical sensing and remediation of 4-nitrophenol. Photocatalytic and antibacterial properties of CuO NPs biosynthesized using *Verbascum thapsus* leaf extract has been reported by Getu et al. [22]. In a study by Azam et al. [23], CuO NPs were reported to exhibit antimicrobial properties that depend on their size. Antioxidant and DNA cleavage properties have been reported for green synthesized CuO NPs by Duman et al. [24].

There are several reasons why CuO is preferred over  $MnO_2$  loading, including its large specific surface area, chemical stability, non-toxicity, high conductivity, and remarkable electrochemical properties [25]. Because of the synergistic effects and morphological structures of  $MnO_2$  and CuO, the  $MnO_2/CuO$  nanocomposite seems to be ideal material for catalysis and antimicrobial applications. With CuO introduction into  $MnO_2$  matrix as reinforcing element, the  $MnO_2/CuO$  NC exhibited improved capacitive performance [26]. Researchers Zhang et al. [27] and CuO et al. [28] have developed  $CuO@MnO_2$  core-shell nanostructures with high supercapacitive performance.  $MnO_2/CuO$  catalyst for co oxidation has been synthesized by Qian et al. [29]. Supercritical oxidative degradation of ethyl acetate in water has been reported by Martin et al. [30]. Lithium-ion batteries with  $CuO@MnO_2$  core-shell nanosheet arrays synthesized by Qing et al. [31] have been found to exhibit high performance.

In spite of the good synergistic effects between  $MnO_2$  and CuO, the photodegradation efficiency is somewhat reduced due to the different oxidation states of  $MnO_2$  and the low band gap value of CuO. To overcome this limitation, rGO is incorporated into the  $MnO_2/CuO$  matrix. The surface of the  $sp^2$ -C atoms in rGO is adorned with oxygenated functional groups and defect sites, giving it a distinctive 2D honeycomb structure. With its variable band gap and exceptional mechanical, chemical, and thermal capabilities, rGO is well suited for composite functioning [32]. Therefore, rGO incorporation is expected to

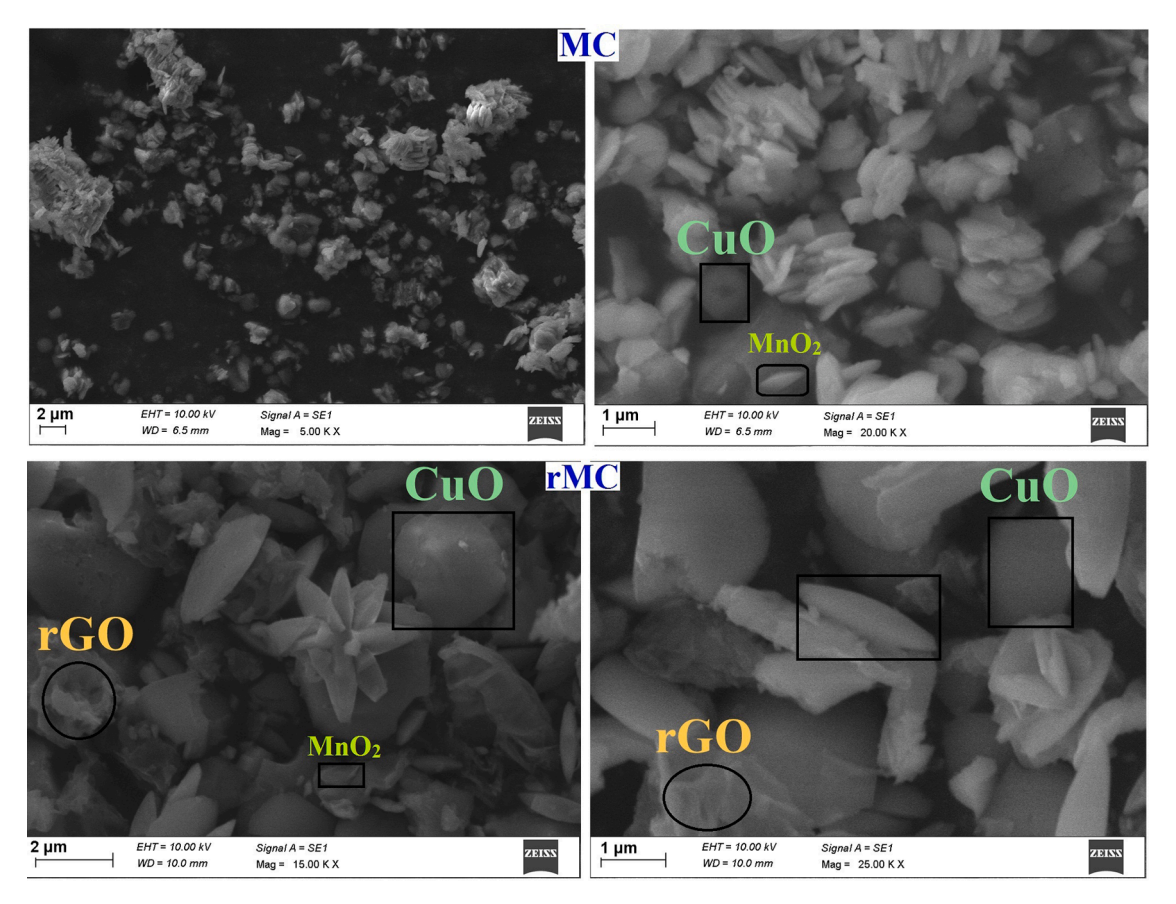


Fig. 3. SEM images of MC and rMC composites

significantly improve the catalytic and antibacterial properties of  $MnO_2/CuO$  nanocomposite. Studies on the electrochemical, catalytic and antibacterial properties of rGO embedded  $MnO_2/CuO$  is very scarce in the literature and the results obtained for the rGO incorporated  $MnO_2/CuO$  NC in this work will address the current research gaps or challenges that arise while utilizing this composite.

#### 2. Experimental

## 2.1. Materials Used

The materials used included graphite powder (purity 98%), sulfuric acid (purity 98.5%), potassium permanganate (purity 99%), phosphoric acid (purity 99%), hydrochloric acid (purity 98%), hydrogen peroxide (purity 99%), manganese chloride (purity 99.6%), cupric chloride (purity 99.2%). An extract of Alternanthera sessilis leaf was used to reduce graphene oxide to rGO.

#### 2.2. Synthesis of MnO<sub>2</sub>/CuO (MC) composite

280~mL of demineralized water and 5 mL of weak hydrochloric acid were added to a 500~ml beaker with 0.1 M manganese (II) chloride and cupric chloride. The mixture was stirred rapidly until the salts were dissolved. After adding 15 mL of liquid NH $_{\! 3}$ , the solution's pH was neutralised and allowed to mature for 12 hours. Finally, MC nanocomposite was obtained by crushing the precipitates after they had been rinsed and calcined at  $400^{\circ}\text{C}$  for 2 hours.

#### 2.3. Synthesis of graphene oxide (GO)

In a 500 mL beaker containing a 9:1 volume mixture of phosphoric acid and sulphuric acid, graphite powder (1 g) was gradually added and

thoroughly mixed while on ice. A constant stirring was performed while potassium permanganate (6 g) was gradually added. For 12 hours, the solution's temperature was raised steadily to  $50^{\circ}\text{C}$  while being vigorously stirred. 800 mL of frozen water and 1 mL of 30% hydrogen peroxide progressively diluted the mixture. Three rounds of washing with deionized water and 10% HCl neutralized the pH. By washing with ethanol and drying for 12 hours at  $60^{\circ}\text{C}$ , brown GO powder was obtained.

#### 2.4. Leaf extract preparation

At 95°C, 10 g of cleaned *Alternanthera sessilis* leaves were cooked for 45 minutes in 200 mL of water. After filtering the solution, the obtained extract was kept at 4°C in the fridge.

#### 2.5. Synthesis of rMC composite

A mixture of 100 mL distilled water and 100 mg (optimized value) of GO powder was mixed before ultrasonically treating for 30 minutes. Thirty minutes after adding MnO $_2$ /CuO precipitates, the mixture was stirred. Afterwards, 25 mL of extract was added and mixed for five hours at 95°C. The concoction was filtered as soon as it reached ambient temperature. After being cleaned and dried for five hours at 80°C, rGO-MnO $_2$ /CuO (rMC) nanocomposite was created. Fig. 1 illustrates the entire synthesizing process.

#### 2.6. Characterization

The chemical structure, morphology, optical nature and luminescence properties were studied using X-ray diffractometer (PRO Analytical X' pert), scanning electron microscope (S-3000H HITACHI), spectrophotometers (Lambda-35) and Varian Cary Eclipse. Functional

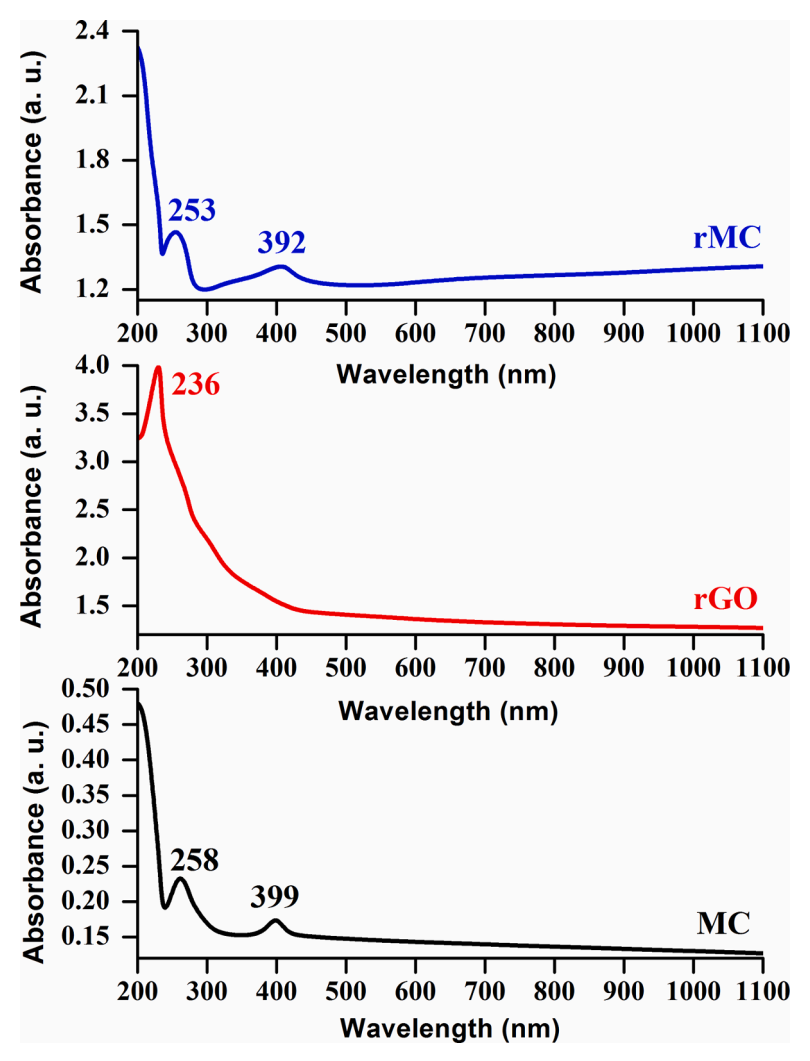
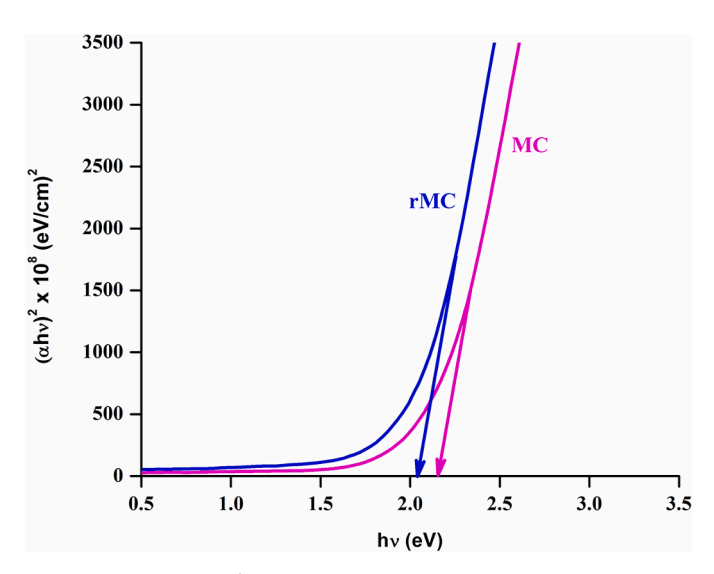


Fig. 4. Absorbance spectra of MC and rMC composites



**Fig. 5.**  $(\alpha h \nu)^2$  vs.  $h \nu$  plots of MC and rMC composites

groups and Raman analyses were performed using spectrophotometers (Perkin Elmer RX-1 and Renishaw Invia Laser).

#### 2.7. Photocatalytic test

MC and rMC catalysts were evaluated for their ability to degrade metanil yellow dye under visible light. In 100 mL water, 0.05 g of MY dye was dissolved and swirled for 30 minutes with and without the catalysts of 6 mg concentration. As visible source, incandescent bulb with a power output of 100 W was used. For every 15 min, absorption spectra was recorded for the dye solution at  $\lambda=435\ nm$ .

#### 2.8. Antibacterial activity

MC and rMC NCs were tested against *Pseudomonas Aeruginosa* (*P. aeruginosa*) bacteria using agar well diffusion method. Bacterial culture was spread over the petriplates containing freshly prepared Muller – Hinton agar medium. Two mg each of the control (Amikacin), MC and rMC NPs were dissolved in 25  $\mu L$  DMSO and incubated at 37° C for 24 hours.

#### 3. Outcomes of the findings

## 3.1. X-ray diffraction studies

The orthorhombic structure of MnO2 [JCPDS No. 82-2169] was

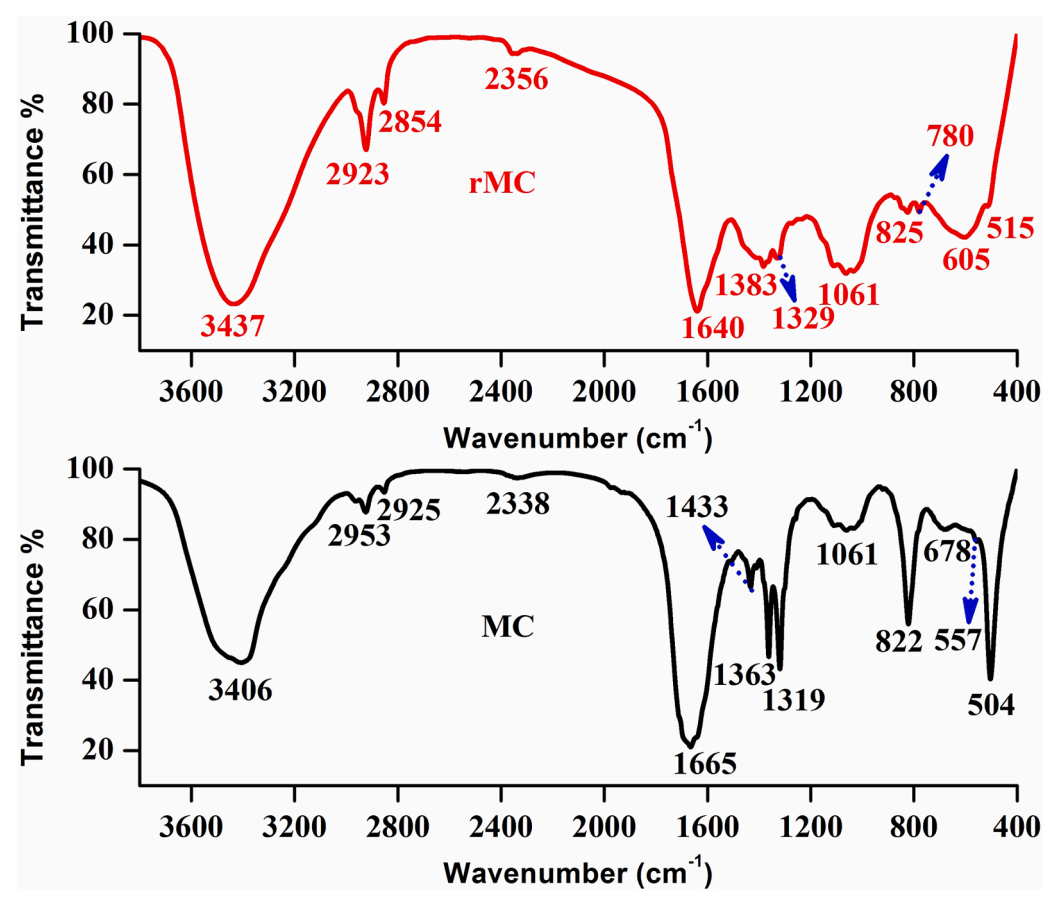


Fig. 6. FTIR spectra of MC and rMC composites

coincident with the peaks (2 0 0), (1 1 0), (2 1 0), (0 1 1), and (4 1 0) denoted by \* (Fig. 2). The monoclinic structure of CuO [JCPDS No. 41-0254] was coincident with the diffraction peaks (1 1 0), (0 0 2), (1 1 1), (1 1 2), and (0 2 0) denoted by the symbol # (Fig. 2). The observed peaks for both composites clearly show MnO2 and CuO coexistence. rGO exhibited a broad (0 0 2) peak at around 24.8° (Fig. 2). However, no peaks related to rGO were observed in the rMC composite due to its weaker intensity than that of MnO2 and CuO [33]. The average crystallite size of MC and rMC composites was 42 and 33 nm, respectively, according to Scherrer's equation. Consistent with previous findings [34], the rMC composite was shown to have smaller crystallites. Malik et al. [35] observed a similar reduction in crystallite size for rGO-ZnO composite, which they attributed to ZnO crystal nucleation disturbances. With decreased crystallite size, the rMC composite exhibits a high surface-to-volume ratio, which could have enhanced its photocatalytic activity (Section 3.6).

#### 3.2. SEM analysis

Fig. 3 shows the SEM images with two different magnifications of MC and rMC nanocomposites. Clustered tiny nanorods with different sizes are seen for the MC composite. Star shaped nanostructures are seen for the rMC composite. Thus, with rGO incorporation morphology of the MC composite changes significantly. Observed star-shaped structure for the rMC composite inhibits self-aggregation, as well as the creation of a larger surface area and more active sites, increasing the production of reactive oxygen species and enhancing its catalytic and antibacterial properties.

#### 3.3. UV-Vis analysis

The absorbance peaks at 258 and 399 nm observed for the MC composite got shifted to 253 and 392 nm with rGO incorporation which exhibited absorbance peak at 236 nm (Fig. 4). Similar shifting of absorbance peaks towards smaller wavelengths with rGO incorporation has been reported earlier [36]. Since rGO has a non-zero visible absorption, rMC composites containing rGO have increased absorption in the visible range. The band gap energies (Eg) of the MC and rMC nanocomposites was calculated using absorption coefficient ( $\alpha$ ) and photon energy ( $h\nu$ ) via Tauc plot method with the equation:

$$\left(\alpha h \nu\right)^2 = \left(h \nu - E_g\right) \tag{1}$$

The calculated  $E_g$  values are 2.16 and 2.04 eV, respectively for the MC and rMC composites (Fig. 5). Oxygen vacancies and strong interfacial interaction between rGO and  $MnO_2/CuO$  nanoparticles may be responsible for the synergistic impact reported in the rMC composite, resulting in a smaller band gap [37]. RMC composite's reduced band gap can also be attributed to surface charge and electronic coupling between  $MnO_2/CuO$  and rGO [38]. Due to decreased band gap, antibacterial activity of the rMC composite is enhanced due to more ROS generation (Section 3.7).

#### 3.4. Functional group analysis

In FT-IR spectra of MC and rMC (Fig. 6) O-H bending occurs at 3406 and 3437 [39]. C-H stretching occurs at 2953 and 2925 cm<sup>-1</sup> for MC and at 2923 and 2854 cm<sup>-1</sup> for rMC [40]. The 2338 and 2356 peaks correspond to HCC=H stretching. The absorption that occurs at a frequency of 1665 cm<sup>-1</sup> in MC can be traced back to the bending vibration of O-H atoms that are connected with Mn atoms [41]. Adding rGO

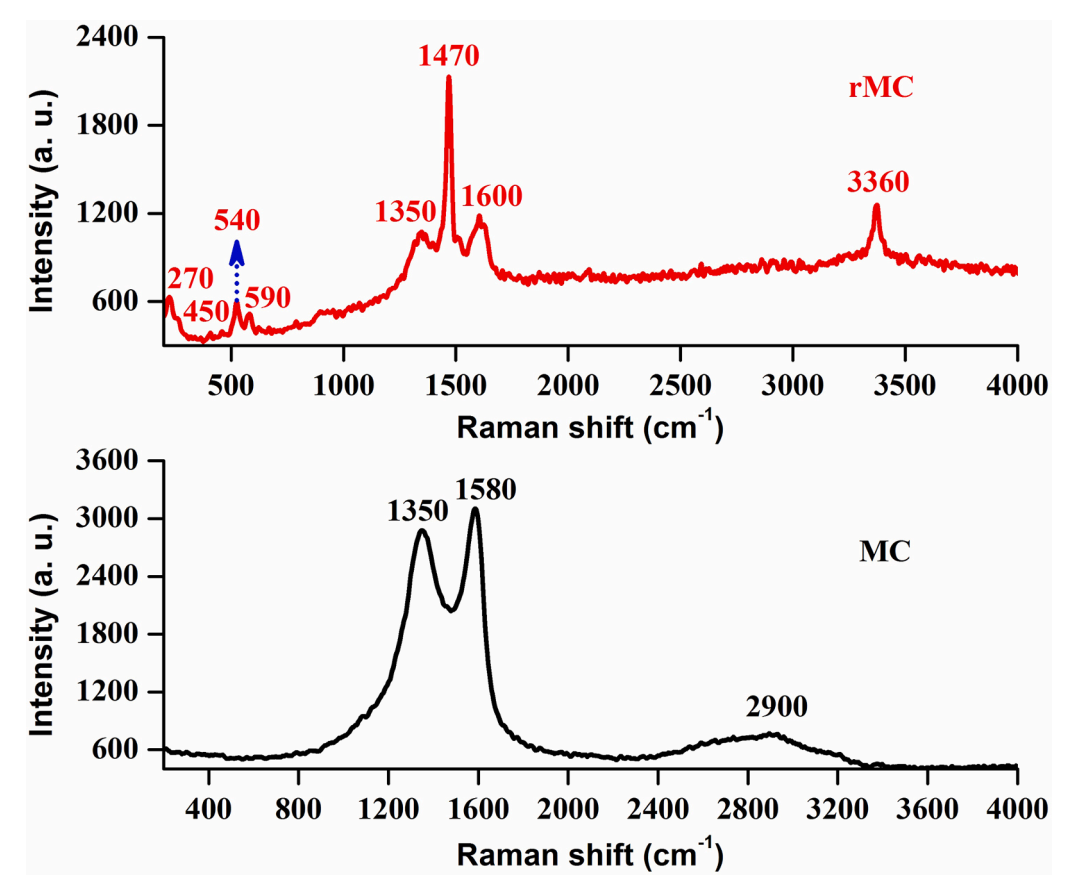


Fig. 7. Raman spectrum of rMC nanocomposite

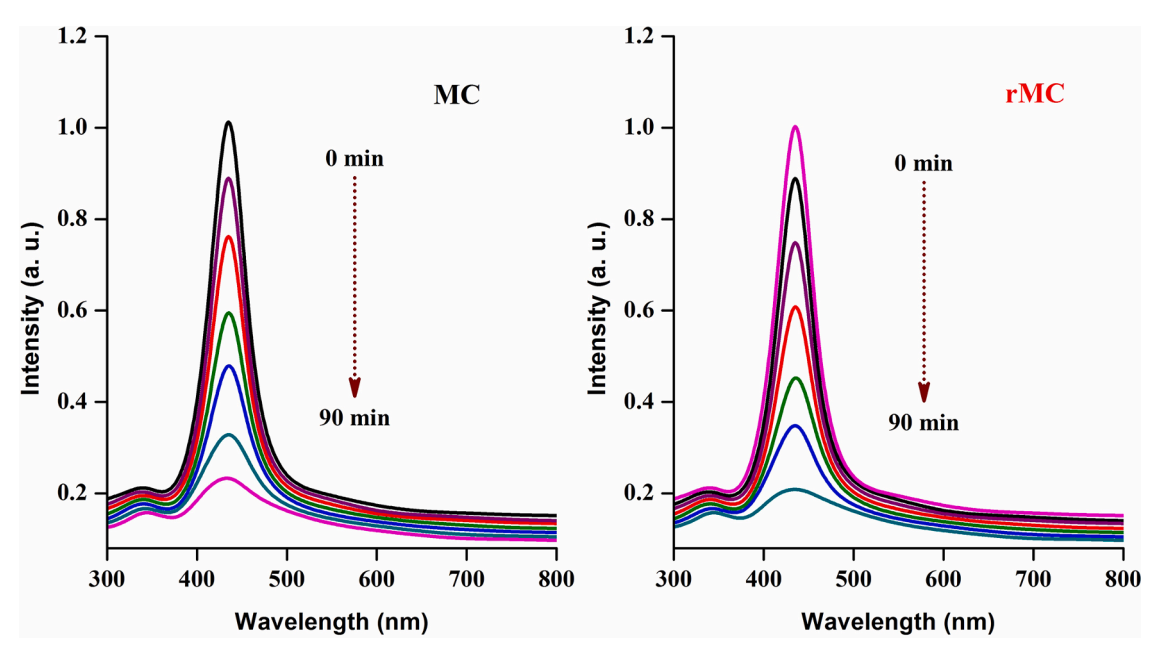


Fig. 8. Absorption spectra of MC and rMC catalysts

caused this peak to move to 1640 cm<sup>-1</sup>. A band at 1433 was detected for the MC composite, and it was shown to be due to the anti-symmetric vibration of adsorbed CO<sub>2</sub> [42]. C–OH vibration occurs at 1363, 1319 cm<sup>-1</sup> for MC and at 1383, 1329 cm<sup>-1</sup> for rMC composites. C–O bond occurs at 1061 cm<sup>-1</sup> [40]. The MC peak at 822 cm<sup>-1</sup> correlates with Mn-O vibrations, which shift to 825 cm<sup>-1</sup> in the rMC [43]. The O-Mn-O

vibrational mode occurs at 780 cm<sup>-1</sup> in the rMC composite [44]. The MC composite has a CuO-related peak at 678, 557 and the rMC composite at 605 cm<sup>-1</sup> [45]. The MC composite's peak at 504 cm<sup>-1</sup> caused by Mn-O-Mn symmetric stretching vibration shifted to 515 cm<sup>-1</sup> for rMC [46].

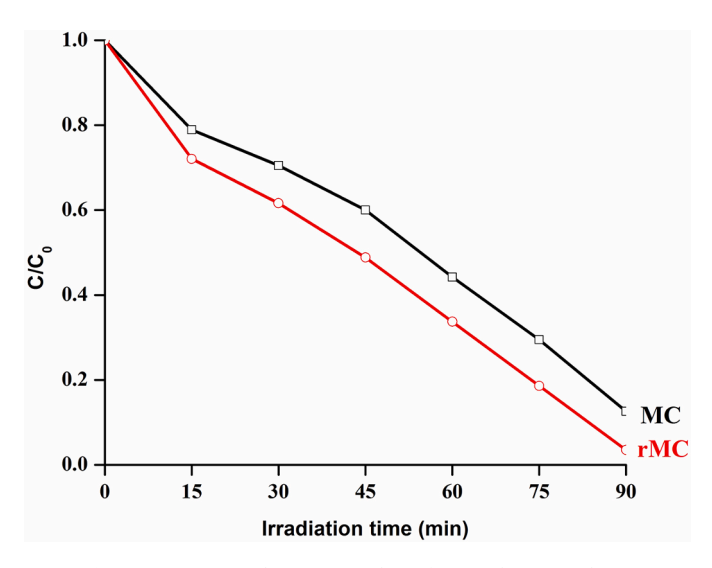


Fig. 9.  $C/C_0$  vs. irradiation time plots of MC and rMC catalysts

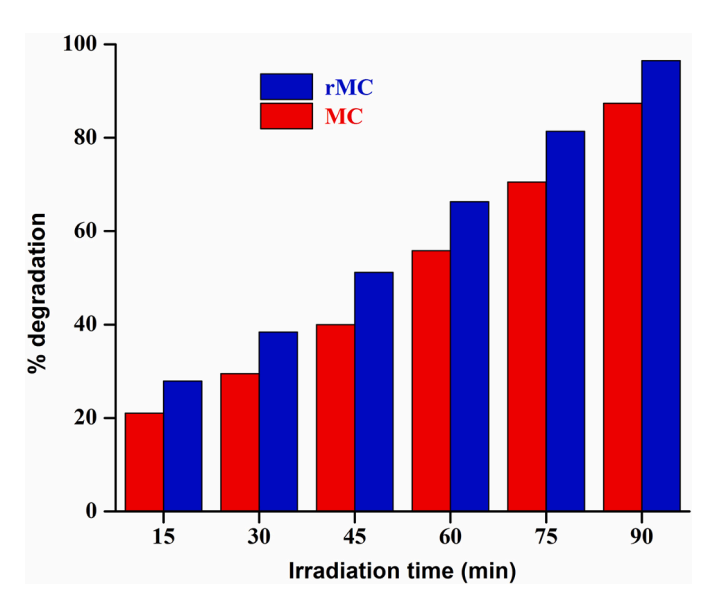


Fig. 10. Photodegradation efficiencies of MC and rMC catalysts

#### 3.5. Raman studies

A prominent peak at 3360 appears in the Raman spectrum of rMC NC (Fig. 7) resulting from the OH stretching vibrations of moisture and rGO [47]. rGO D and G bands are represented by the 1350 and 1600 cm $^{-1}$  peaks, respectively [48]. The D band is an indication that there are faults in the atomic layers that make up the graphite, whereas the G band is the result of the stretching of in-plane bonds between sp $^2$ C atoms [49]. The C-O stretching vibration of rGO causes the peak at 1470 [50]. Peaks at 590 and 540 [51] are due to Mn-O symmetric vibrations. Raman active  $\rm A_g$  and  $\rm B_g$  CuO modes occur at 270 and 450 cm $^{-1}$  [52]. Thus, the rMC nanocomposite contains the Raman characteristic bands of rGO, MnO $_2$  and CuO materials.

#### 3.6. Photocatalytic test

The UV-Vis spectra of MY with MC and rMC catalysts are depicted in Fig. 8. It is discovered that MY's 435 nm distinctive absorption rapidly declines with exposure to visible light and nearly vanishes after 90 minutes. The spectral absorption peak is eliminated by additional

**Table 1**Comparison on the photodegradation efficiencies of rMC catalyst with other rGO based composites

Composite	Dye	Light Source	Irradiation time	Degradation efficiency	Reference
CdO/ CeO <sub>2</sub> / RGO	МО	Ultrasonic irradiation	150 min	85 %	[56]
PANI/ rGO/ MnO <sub>2</sub>	MB	Visible	120 min	91%	[57]
TiO <sub>2</sub> / RGO/Ag	MB	UV	90 min	81%	[58]
ZnO/ CdO/ rGO	MO, RhB	Ultrasonic irradiation	120 min	84, 80 %	[59]
rGO/ CdO/ SnO <sub>2</sub>	CR, MG	Visible	120 min	82%, 94%	[60]
WO <sub>3</sub> / CuO/ rGO	RhB	Visible	90 min	93%	[61]
rGO- MnO <sub>2</sub> / CuO	MY	Visible	90 min	96%	This work

exposure, demonstrating complete decay of MY. Y<sup>3+</sup> and Sm<sup>3+</sup> co-doped NiO nanocomposite reported by Kannan et al. [53] are consistent with this. Fig. 9 shows the results of MY degradation under the condition of MC and rMC catalysts. Without the catalyst, the MY concentration drops very slightly when subjected to irradiation in a blank test.

The degradation percentage of MY solutions using MC and rMC catalysts for 90 min is 87 and 96 %, respectively (Fig. 10). This clearly indicates that with rGO incorporation, the photodegradation ability of MC nanocomposite is enhanced substantially. The introduction of rGO into the MC catalyst enhanced the surface area, which led to a greater degrading efficiency. rGO's higher surface area and more active areas lower electron and hole recombination [34]. rGO addition enhances the MC catalyst's light absorption via the  $\pi$ - $\pi$  stacking interface and increased degradation efficiency [42]. The reduced band gap and star morphology of the rMC catalyst also contributed to its degradation efficiency [55]. A comparison on the degradation efficiency of the rMC catalyst with previously reported rGO decorated nanocomposites is compiled in Table 1.

The  $E_{CB}$  and  $E_{VB}$  potentials of MnO $_2$  and CuO computed using the following relations can be used to explore the photocatalytic mechanism involved in the rMC catalyst:

$$E_{VB} = X - E^e + 0.5 E_e \tag{2}$$

$$E_{CB} = E_{VB} - E_g \tag{3}$$

MnO $_2$  and CuO have  $E_{CB}$  values of -0.757 and 0.24 eV and  $E_{VB}$  values of 1.563 and 2.05 eV, respectively, according to calculations. The higher positive edge potential of CuO contributes to its stronger oxidative ability, thus dominating the photocatalytic activity of MnO $_2$ /CuO. The photocatalytic mechanism of the rMC catalyst is illustrated in Fig. 11. As the CB potential of MnO $_2$  is negative, electrons diffuse from the CB of MnO $_2$  to CuO through rGO under visible light exposure. Similarly, holes diffuse from the VB of CuO to MnO $_2$  through rGO. As a result, charge carriers are effectively segregated, lengthening their life time and improving interfacial charge transfer efficiency. Complete mineralization of MY occurred when photogenerated electrons were neutralised by dissolved oxygen molecules in water, creating  $O_2^{*-}$  radicals, and photogenerated holes interacted directly with H $_2$ O to create OH $^*$  radicals [54].

The photodegradation rate constants (k) of MC and rMC catalysts were investigated usiong the relation:

$$k = \frac{\ln(C_0/C)}{t} \tag{4}$$

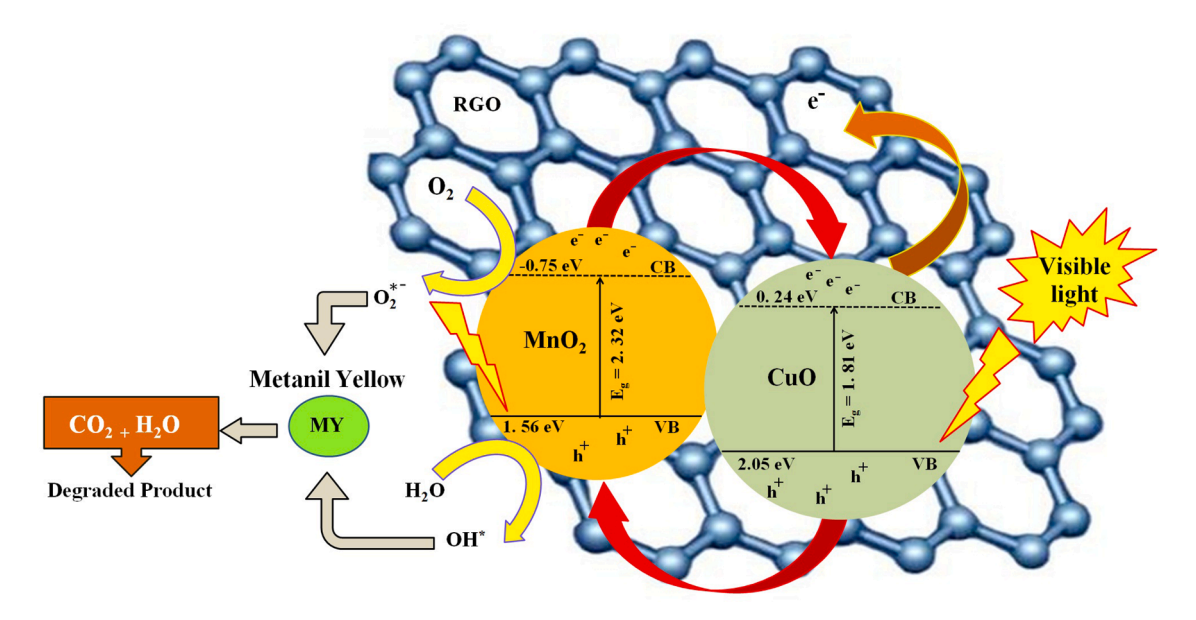


Fig. 11. Photocatalytic mechanism of rMC catalyst

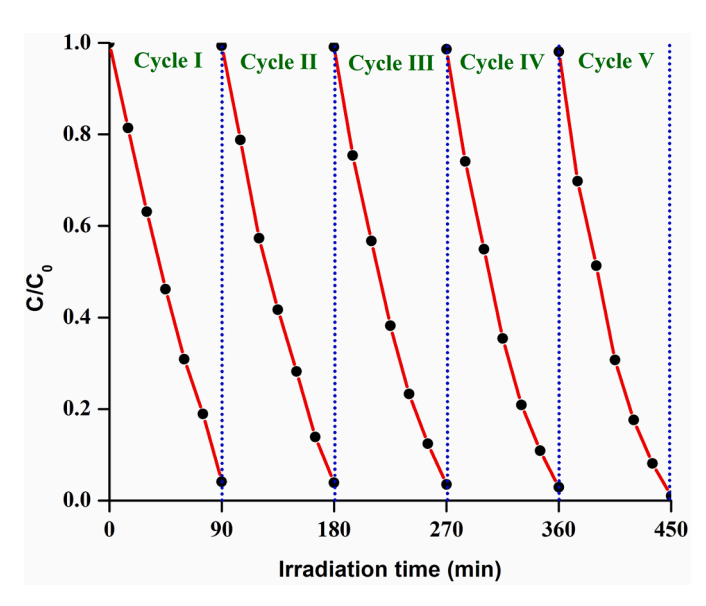


Fig. 12. Recycle test of rMC catalyst

where  $C_0$  and C are the dye concentration under dark and light conditions. The k values estimated from the plots between  $\ln(\frac{C_0}{C})$  vs. irradiant time were 0.0157 and 0.0284 min $^{-1}$  for the MC and rMC catalysts, respectively. rMC catalyst's high k value confirmed its higher degradation capability.

The recyclability of the rMC catalyst was examined by doing the degradation experiment five times. Recycle experiments of the rMC catalyst with MY are shown in Fig. 12. No discernible efficiency loss was seen for the first four cycles, but an abnormal efficiency decline was seen for the fifth. The acquired results validated the photocatalyst's remarkable stability, which is further substantiated by the FTIR spectrum (Fig. 13) of the recovered photocatalyst.

#### 3.7. Antibacterial activities

MC and rMC nanocomposites were tested for their antibacterial activity against P. aeruginosa bacteria. The antibacterial activity was

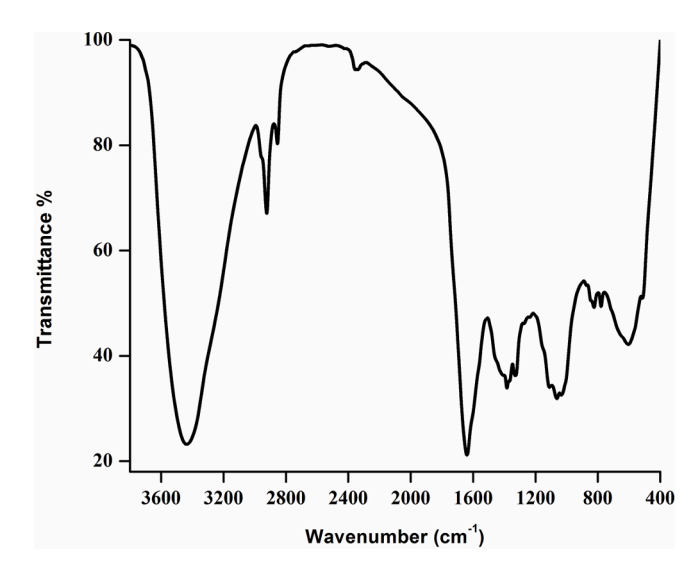


Fig. 13. FTIR spectrum of recycled rMC catalyst

studied with an optimum concentration of the composites ( $25\mu L$ ). The measured ZOI values (Fig. 14) are 13, 18 and 24 mm for the control (Amikacin), MC and rMC nanocomposites. As shown in Table 2, rMC NC has superior antibacterial performance when compared with previously reported rGO nanocomposites.

The MC and rMC composites resisted the bacterial growth effectively better than the control. The highest ZOI observed for the rGO-MnO $_2$ /CuO nanocomposite confirmed its best potentiality against the tested bacteria. Metal ion release (Mn $^{2+}$ , Cu $^{2+}$ ), reactive oxygen species production (H $_2$ O $_2$ , OH $^*$ , O $_2$ \* $^-$ ), and the surface area of the composites were all cited as contributing to the composites' antibacterial activity [66]. O $_2$ \* $^-$  is one type of ROS that is harmful to numerous cellular components like nucleic acid, lipids, proteins, DNA, and carbohydrates [67]. The bacterial cell is extremely sensitive to the severe oxidative effects of both H $_2$ O $_2$  and OH $^*$  radicals. As a result, several crucial biological functions of the cell are harmed, which may prevent cell division and growth [68]. According to Kannan et al. [69], lipid peroxidation, DNA damage, and protein oxidation all cause bacteria to die, but not nonbacterial cells. Freed metal ions are attracted by the thiol groups

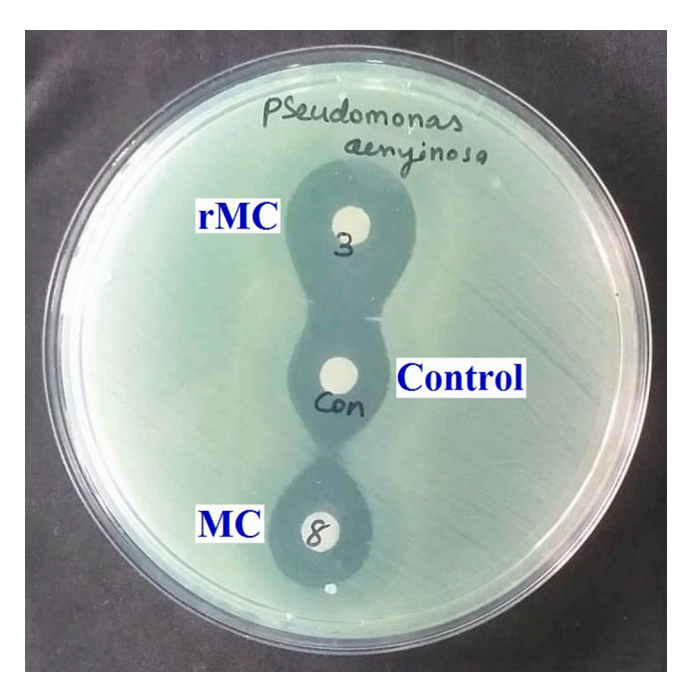


Fig. 14. Antibacterial activity of control, MC and rMC nanocomposites

**Table 2**Comparison on the antibacterial performance of rMC NC with previously reported rGO based nanocomposites

Composite	Bacteria	ZOI (mm)	Reference
rGO-WO <sub>3</sub> /CuO	Klebsiella pneumoniae	2	[61]
Palladium-rGO/ZnO	Pseudomonas aeruginosa	16	[62]
RGO-Ag/ZnO	Escherichia coli	16	[63]
rGO-SnO <sub>2</sub> -NiO-CuO	Staphylococcus aureus	16	[64]
La <sub>2</sub> CuO <sub>4</sub> / CeO <sub>2</sub> /rGO	Escherichia coli	16	[65]
rGO-MnO <sub>2</sub> /CuO	Pseudomonas aeruginosa	24	This work

(-SH) on the outer surface proteins of the cell membrane, which damages the membrane by denaturement of the proteins [70]. Differences in antibacterial activity between MC and rMC NCs are due to their size or ROS generation capacity. More ROS were generated due to the smaller crystallite size and band gap found for the rMC nanocomposite, leading to improved antibacterial activity. In addition, the rGO in the MC composite triggers a chain reaction of biological processes that ultimately kills the bacteria. When bacteria come into touch with rGO, they frequently experience a loss of cell membrane integrity. Graphene-based nanoparticles can lower mitochondrial membrane potential, resulting in increased ROS generation and death through activation of the mitochondrial pathway [71]. A graphene-based nanomaterial's interactions with genetic material are usually caused by DNA intercalation and breakage. Therefore, nanoparticles made of graphene interact directly with certain genes that code for important enzymes and proteins [72]. The antibacterial activity of the rMC nanocomposite is represented in Fig. 15.

#### 4. Conclusion

NCs of MnO<sub>2</sub>/CuO and rGO-MnO<sub>2</sub>CuO were prepared through chemical precipitation and one-pot green synthesis. Leaf extract from the plant *Alternanthera sessilis* was used to transform graphene oxide made using Hummer's technique into rGO. Comparison on the structural, optical, photocatalytic and antibacterial properties of MnO<sub>2</sub>/CuO composite with that of rGO-decorated MnO<sub>2</sub>/CuO composite is very scarce and this work presented the comparative results obtained. The rMC composite exhibited smaller crystallites. Within 90 minutes, the MC and rMC nanocomposites destroyed roughly 87 and 96% of the metanil yellow dye, respectively. rGO-MnO<sub>2</sub>/CuO nanocomposite showed improved antibacterial activity. Thus, MnO<sub>2</sub>/CuO nanocomposite incorporated with rGO showed good antimicrobial properties and efficiently degraded toxic metanil yellow dye.

#### Statements and Declarations

#### Funding

No funding was received to assist with the preparation of this manuscript.

#### Authors' contributions

Conceptualization - Dr. S. Jothi Ramalingam; Methodology - Mr. A. Ceril Jeoffrey; Formal analysis and investigation - Dr. A.R. Balu; Writing - original draft preparation - K. Murugaiah; Writing -

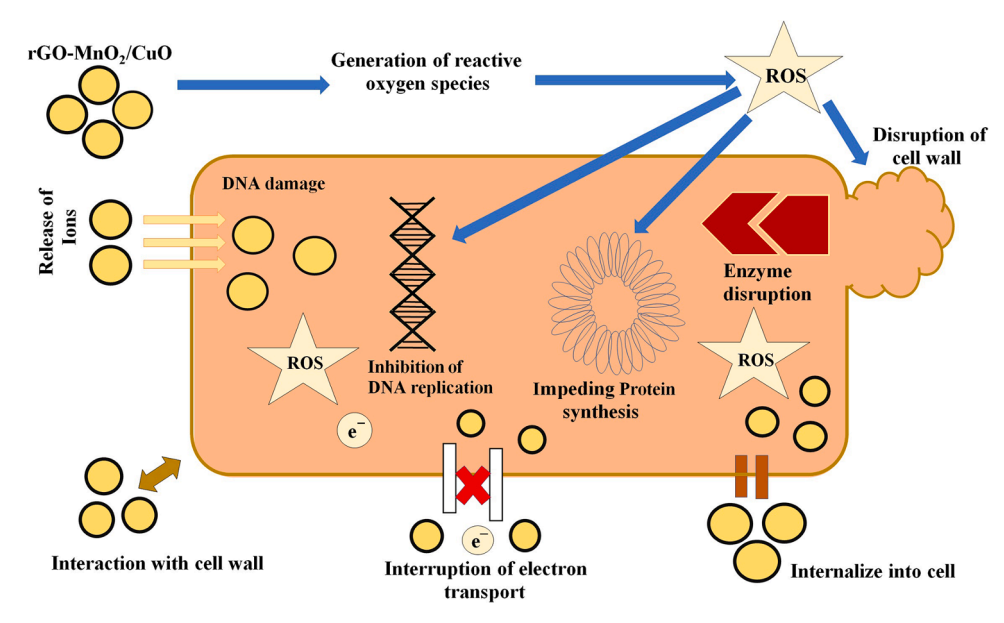


Fig. 15. Schematic representation of antibacterial resistance of rMC composite

**review and editing** – Dr. A.R. Balu; **Funding acquisition** - Dr. Ceril Jeoffrey; **Interpretation of data** - Dr. S. Jothi Ramalingam.

The final manuscript was read and approved by all authors.

#### **Declaration of Competing Interest**

The authors declare that they have no known competing financial interests or personal relationships that could have appeared to influence the work reported in this paper.

#### Data availability

No data was used for the research described in the article.

#### Acknowledgements

For Raman studies, we are very thankful to Alagaappa University, Karaikudi.

#### References

- [1] Z. Cai, Y. Sun, W. Liu, F. Pan, P. Sun, J. Fu, An overview of nanomaterials applied for removing dyes from wastewater, Environ. Sci. Pollut. Res. Int. 24 (2017) 15882–15904, https://doi.org/10.1007/s11356-017-9003-8.
- [2] N. Ahmad, S. Sultana, S. Sabir, M.Z. Khan, Exploring the visible light driven photocatalysis by reduced graphene oxide supported Ppy/CdS nanocomposites for the degradation of organic pollutants, J. Photochem. Photobiol. A. Chem. 386 (2020), 112129, https://doi.org/10.1016/j.jphotochem.2019.112129.
- [3] R. Nallendran, G. Selvan, A.R. Balu, CdO-Fe<sub>3</sub>O<sub>4</sub> nanocomposite with enhanced magnetic and photocatalytic properties, Mater. Sci. Poland 37 (2019) 100–107, https://doi.org/10.2478/msp-2019-0012.
- [4] K. Tantubay, P. Das, M. Baskey Sen, Ternary reduced graphene oxide-CuO/ZnO nanocomposite as a recyclable catalyst with enhanced reducing capability, J. Environ. Chem. Eng. 8 (2020), 103818, https://doi.org/10.1016/j.iogg.2020.103818
- [5] Z.M. Shammi, A.H. Kianfar, M.M. Momeni, Hydrothermal synthesis and characterization of CuO-CoO/TiO<sub>2</sub> for photocatalytic degradation of methylene blue under visible light and catalytic reduction of p-nitrophenol, J. Mater. Sci. Mater. Electron. 31 (2020) 14810–14822, https://doi.org/10.1007/s10854-020-04044.9
- [6] K. Kannan, D. Radhika, A.S. Nesaraj, K.K. Sadasivuni, L.S. Krishna, Facile synthesis of NiO-CYSO nanocomposite for photocatalytic and antibacterial applications, Inorg. Chem. Commun. 122 (2021), 108307, https://doi.org/10.1016/j. inoche.2020.108307.
- [7] N. Manjula, G. Selvan, A.R. Balu, Photocatalytic Performance of SnO<sub>2</sub>:Mo nanopowders against the degradation of methyl orange and rhodamine B dyes under visible light irradiation, J. Electron. Mater. 48 (2019) 401–408, https://doi.org/10.1007/s11664-018-6720-9.
- [8] G. Shanmugavel, A.R. Balu, V.S. Nagarethinam, S. Ravishankar, M. Suganya, S. Balamurugan, K. USharani, C. Kayathiri, M. Karthika, CdO:Ag thin films with enhanced visible light photocatalytic activity against metanil yellow, SN Appl. Sci. 1 (2019) 1203, https://doi.org/10.1007/s42452-019-1237-2.
- H. Xu, W. Wang, W. Zhu, Shape evolution and size-controllable synthesis of Cu<sub>2</sub>O octahedra and their morphology-dependent photocatalytic properties, J. Phys. Chem. B 110 (2006) 13829–13834, https://doi.org/10.1021/jp061934y.
- [10] K. Ramesh, L. Chen, F. Chen, Y. Liu, Z. Wang, Y.F. Han, Re-investigating the co oxidation mechanism over unsupported MnO, Mn<sub>2</sub>O<sub>3</sub> and MnO<sub>2</sub> catalysts, Catal. Today 131 (2008) 477–482, https://doi.org/10.1016/j.cattod.2007.10.061.
- [11] L. Chen, R. Huang, Y.J. Ma, S.L. Luo, C.T. Au, S.F. Yin, Controllable synthesis of hollow and porous Ag/BiVO<sub>4</sub> composites with enhanced visible-light photocatalytic performance, RSC Adv 3 (2013) 24354–24361, https://doi.org/ 10.1039/C3RA43691H.
- [12] M. Huang, F. Li, F. Dong, Y.X. Zhang, L.I. Zhang, MnO<sub>2</sub>-based nanostructures for high performance supercapacitors, J. Mater. Chem. 3 (2015) 21380–21423, https://doi.org/10.1039/C5TA05523G.
- [13] L. Liu, Y. Luo, W. Tan, Y. Zhang, F. Liu, G. Qiu, Facile synthesis of birnessite-type manganese oxide nanoparticles as supercapacitor electrode materials, J. Colloid Interface sci. 482 (2016) 183–192, https://doi.org/10.1016/j.jcis.2016.07.077.
- [14] M. Sun, B. Lan, T. Lin, G. Cheng, F. Ye, L. Yu, Controlled synthesis of nanostructured manganese oxide: crystalline evolution and catalytic activities, CrystEngComm 15 (2013) 7010–7018, https://doi.org/10.1039/C3CE40603B.
- [15] J. Chen, X. Chen, Z. Xu, W.J. Xu, J.J. Li, H.P. Jia, J. Chen, Syntheses of hierarchical MnO<sub>2</sub> via H<sub>2</sub>O<sub>2</sub> selectively reducing KMnO<sub>4</sub> for catalytic combustion of toluene, Chemistry 1 (2016) 4052–4056, https://doi.org/10.1002/slct.201600921.
- [16] Y. Chen, D. Ye, M. Wu, H. Chen, L. Zhang, J. Shi, L. Wang, Break-up of twodimensional MnO<sub>2</sub> nanosheets promotes ultrasensitive ph-triggered theranostics of cancer, Adv. Mater 26 (2014) 7019–7026, https://doi.org/10.1002/ adma.201402572.

- [17] Y. Chen, H. Cong, Y. Shen, B. Yu, Biomedical application of manganese dioxide nanomaterials, Nanotechnol 31 (2020), 202001, https://doi.org/10.1088/1361-6528/ab6fe1.
- [18] A. Nezamzadsh-Ejhieh, M. Amiri, CuO supported clinoptilolite towards solar photocatalytic degradation of p-aminophenol, Powder Technol 235 (2015) 279–288, https://doi.org/10.1016/j.powtec.2012.10.017.
- [19] S.A. Akintelu, A.S. Folorunso, F.A. Folorunso, A.K. Oyebamiji, 2020. Green synthesis of copper oxide nanoparticles for biomedical application and environmental remediation. Heliyon. 6, e04508. doi:10.1016/j.heliyon.2020.e0 4508.
- [20] S. Rajeswari, K.S.M.R. Pattanathu, R. Rajiv, A.S. Hasna, R. Venkatesh, Biogenic copper oxide nanoparticles synthesis using *Tabernaemontana divaricate* leaf extract and its antibacterial activity against urinary tract pathogen, Spectrochim. Acta Mol. Biomol. Spectrosc. 133 (2014) 178–181, https://doi.org/10.1016/j.ssa.2014.05.048.
- [21] S. Singh, N. Kumar, M. Kumar, J.A. Agarwal, B. Mizaikoff, Electrochemical sensing and remediation of 4-nitrophenol using bio-synthesized copper oxide nanoparticles, Chem. Eng. J. 313 (2017) 283–292, https://doi.org/10.1016/j. cej.2016.12.049.
- [22] K.W. Getu, Photocatalytic and antibacterial activity of CuO nanoparticles biosynthesized using *Verbascum thapsus* leaves extract, Optik 204 (2020), 164230, https://doi.org/10.1016/j.ijleo.2020.164230.
- [23] A. Azam, A.S. Ahmed, M. Oves, M.S. Khan, A. Memic, Size-dependent antimicrobial properties of CuO nanoparticles against Gram-positive and -negative bacterial strains, Int. J. Nanomed. 7 (2012) 3527–3535, https://doi.org/10.2147/ LIN \$29020
- [24] F. Duman, I. Ocsoy, F.O. Kup, Chamomile flower extract-directed CuO nanoparticle formation for its antioxidant and DNA cleavage properties, Mater. Sci. Eng. C. 60 (2016) 333–338, https://doi.org/10.1016/j.msec.2015.11.052.
- [25] A.K. Mishra, A.K. Nayak, A.K. Das, D. Pradhan, Microwave-assisted solvothermal synthesis of cupric oxide nanostructures for high-performance supercapacitor, J. Phys. Chem. C 122 (2018) 11249–11261, https://doi.org/10.1021/acs. ipcc.8b02210.
- [26] B. Padmadevi, A. Pugazhendhi, A.S. Khalifa, R. Shanmuganantham, T. Kalaivani, Novel MnO<sub>2</sub>-CuO-BaO metal oxide nanocomposite for high performance supercapacitors, Proc. Biochem. 110 (2021) 176–180, https://doi.org/10.1016/j. procbio.2021.08.017.
- [27] Y.X. Zhang, F. Li, M. Huang, One-step hydrothermal synthesis of hierarchical MnO<sub>2</sub>-coated CuO flower-like nanostructures with enhanced electrochemical properties for supercapacitor, Mater. Lett. 112 (2013) 203–206, https://doi.org/ 10.1016/j.matlet.2013.09.032.
- [28] X.L. Guo, G. Li, M. Kuang, Y.X.Zhang L.Yu, Tailoring Kirkendall effect of the KCu7S4 microwires towards CuO@MnO<sub>2</sub> core-shell nanostructures for supercapacitors, Electrochim. Acta 174 (2015) 87–92, https://doi.org/10.1016/j. electacta.2015.05.157.
- [29] K. Qian, Z. Qian, Q. Hua, Z. Jiang, W. Huang, Structure–activity relationship of CuO/MnO<sub>2</sub> catalysts in CO oxidation, Appl. Surf. Sci. 273 (2013) 357–363, https://doi.org/10.1016/j.apsusc.2013.02.043.
- [30] A. Martin, U. Armbruster, M. Schncider, J. Radnik, M.M. Pohl, Structural transformation of an alumina-supported MnO<sub>2</sub>-CuO oxidation catalyst by hydrothermal impact of sub and supercritical water, J. Mater. Chem. 12 (2002) 639–645, https://doi.org/10.1039/B107982B.
- [31] C. Qing, B. Heng, H. Wang, D. Sun, B. Wang, M. Sun, S. Guan, R. Fu, Y. Tang, Controlled facile synthesis of hierarchical CuO@MnO<sub>2</sub> core-shell nanosheet arrays for high performance lithium-ion battery, J. Alloys Compnd. 641 (2015) 80–86, https://doi.org/10.1016/j.jallcom.2015.03.234.
- [32] S. Korkmaz, A. Kariper, Graphene and graphene oxide based aerogels: Synthesis, characteristics and supercapacitor applications, J. Energy Storage. 27 (2020), 101038, https://doi.org/10.1016/j.est.2019.101038.
- [33] D. Zhang, H. Chang, P. Li, R. Liu, Characterization of nickel oxide decorated-reduced graphene oxide nanocomposite and its sensing properties toward methane gas detection, J. Mater. Sci. Mater. Electron. 27 (2016) 3723–3730, https://doi.org/10.1007/s10854-015-4214-6.
- [34] A. Irshad, F. Farooq, M.F. Warsi, N. Shabeen, A.Y. Elnaggar, E.E. Hussein, Z.M. El-Bahy, M. Shahid, Ag-doped FeCo<sub>2</sub>O<sub>4</sub> nanoparticles and their composite with flat 2D reduced graphene oxide sheets for photocatalytic degradation of colored and colorless compounds, Flatchem 31 (2022), 100325, https://doi.org/10.1016/j.flatc.2021.100325.
- [35] A.R. Malik, S. Sharif, F. Shaheen, M. Khalid, Y. Iqbal, A. Faisal, M.H. Aziz, M. Atif, S. Ahmad, M.F. Alam, N. Hossain, H. Ahmad, T. Botmart, Green synthesis of rGO-ZnO mediated *Ocimim basilicum* leaves extract nanocomposite for antioxidant, antibacterial, antidiabetic and photocatalytic activity, J. Saudi Chem. Soc. 26 (2022), 101438, https://doi.org/10.1016/j.jscs.2022.101438.
- [36] I. Tanisik, O. Uguz, D. Akyuz, R.M.Z. Ayaz, C. Sarioglu, F. Karaca, A.R. Ozkaya, A. Koca, Solar-hydrogen production with reduced graphene oxide supported Cd<sub>x</sub>Zn<sub>1-x</sub>S photocatalysts, Int. J. Hyd. Energy 45 (2020) 34845–34856, https://doi.org/10.1016/j.ijhydene.2020.04.035.
- [37] R.M. Obodo, H.E. Nsude, C.U. Eze, B.O. Okereke, S.C. Ezugwee, I. Ahmed, M. Maaza, F.I. Ezema, Optimization of MnO<sub>2</sub>, NiO and MnO<sub>2</sub>@ NiO electrodes using graphene oxide for supercapacitor applications, Current Res. Green Sust. Chem. 5 (2020), 100345, https://doi.org/10.1016/j.crgsc.2022.100345.
- [38] X.X. Liu, X. Li, X.X. Liu, S. He, J. Jin, H. Meng, Green preparation of Ag-ZnO-rGO nanoparticles for efficient adsorption and photodegradation activity, Coll. Surf. A Physicochem. Eng. Asp. 584 (2020), 124011, https://doi.org/10.1016/j.colsurfa.2019.124011.

- [39] D.L. Zhao, X. Gao, C.N. Wu, R. Xic, S.J. Feng, C.L. Chen, Facile preparation of amino functionalized graphene oxide decorated with Fe<sub>3</sub>O<sub>4</sub> nanoparticles for the adsorption of Cr (VI), Appl. Surf. Sci. 384 (2016) 1–9, https://doi.org/10.1016/j. apsusc.2016.05.022.
- [40] K. Rahimi, H. Zafarkish, A. Yazdani, Reduced graphene oxide can activate the sunlight-induced photocatalytic effect of NiO nanowires, Mater. Design. 144 (2018) 214–221, https://doi.org/10.1016/j.matdes.2018.02.030.
- [41] K.Mohamed Racik, A. Manikandan, M. Mahendiran, P. Prabakaran, J. Madhavan, M. Victor Antony Raj, Fabrication of manganese oxide decorated copper oxide (MnO<sub>2</sub>/CuO) nanocomposite electrodes for energy storage supercapacitor devices, Physica E 119 (2020), 114033, https://doi.org/10.1016/j.physe.2020.114033.
- [42] S. Sadhukan, A. Battacharya, D. Rana, T.K. Ghosh, J.T. Orasugh, S. Khatua, K. Acharya, D. Chattopadhyay, Synthesis of rGO/NiO nanocomposites adopting a green approach and its photocatalytic and antibacterial properties, Mater. Chem. Phys. 247 (2020), 122906, https://doi.org/10.1016/j.matchemphys.2020.122906.
- [43] C. Wallar, D. Luo, R. Poon, I. Zhitomirsky, Manganese dioxide-carbon nanotube composite electrodes with high active mass loading for electrochemical supercapacitors, J. Mater. Sci. 52 (2017) 3687–3696, https://doi.org/10.1007/ s10853.016.0711.0
- [44] P. Sengodan, R. Govindan, G. Arumugam, B. Chettiannan, M. Navaneethan, M. R. Pallavolu, M. Hussien, M. Selvaraj, R. Rajendran, A rational design of MnO<sub>2</sub>/CuO/r-GO hybrid and biomass-derived activated carbon for asymmetric supercapacitors, J. Energy Storage 50 (2022), 104625, https://doi.org/10.1016/j.est 2022 104625
- [45] A.M. Zardkhoshowi, S.S.H. Davarani, Flexible asymmetric supercapacitors based on CuO @ MnO<sub>2</sub>-rGO and MoS<sub>2</sub>-rGO with ultrahigh energy density, J. Electroanal. Chem. 827 (2018) 221–229, https://doi.org/10.1016/j.jelechem.2018.08.023.
- [46] M. Jayasree, M. Parthibavaraman, R. Boopathi Raja, S. Prabhu, R. Ramesh, Ultrafine MnO<sub>2</sub>/graphene based hybrid nanoframeworks as high-performance flexible electrode for energy storage applications, J. Mater. Sci. Mater. Electron. 31 (2020) 6910–6918, https://doi.org/10.1007/s10854-020-03254-5.
- [47] L.C. Sim, K.H. Leong, S. Ibrahim, P. Saravanan, Graphene oxide and Ag engulfed TiO<sub>2</sub> nanotube arrays for enhanced electron mobility and visible-light-driven photocatalytic performance, J. Mater. Chem. A 2 (2014) 5315–5322, https://doi. org/10.1039/C3TA14857B.
- [48] R. Kumar, S.M. Youssry, H.M. Soe, M.M. Abdel-Galeil, G. Kawamura, Honeycomb-like open-edged reduced-graphene-oxide-enclosed transition metal oxides (NiO/Co<sub>3</sub>O<sub>4</sub>) as improved electrode materials for high-performance supercapacitor, J. Energy Storage. 30 (2020), 101539, https://doi.org/10.1016/j.est.2020.101539.
- [49] R. Kumar, M.M. Abdel-Galeil, K.Z. Ya, K. Fujita, W.K. Tan, A. Matsuda, Facile and fast microwave-assisted formation of reduced graphene oxide-wrapped manganese cobaltite ternary hybrids as improved supercapacitor electrode material, Appl. Surf. Sci. 481 (2019) 296–306, https://doi.org/10.1016/j.apsusc.2019.03.085.
- [50] A.M. Abdelkader, C. Valles, A.J. Cooper, I.A. Kinloch, R.A.W. Dryfe, Alkali reduction of graphene oxide in molten halide salts: production of corrugated graphene derivatives for high-performance supercapacitors, ACS Nano 8 (2014) 11225–11233. https://doi.org/10.1021/nn505700x.
- [51] R.R. Palem, S. Ramesh, C. Bathula, V. Kakani, G.D. Saratale, H.M. Yadav, J.H. Kim, H.S. Kim, S.H. Lee, Enhanced supercapacitive behavior by CuO@MnO<sub>2</sub>/ carboxymethyl cellulose composites, Ceram. Int. 47 (2021) 26738–26747, https:// doi.org/10.1016/j.ceramint.2021.06.081.
- [52] F. Boran, Encapsulation of CuO nanoparticles inside the channels of the multi-walled carbon nanotubes functionalized with thermal stress, Diamond Related Mater 114 (2021), 108306, https://doi.org/10.1016/j.diamond.2021.108306.
- [53] K. Kannan, D. Radhika, D. Gnanasangeetha, L. Sivarama Krishna, K. Gurushankar, Y<sup>3+</sup> and Sm<sup>3+</sup> co-doped mixed metal oxide nanocomposite: Structural, electrochemical, photocatalytic and antibacterial properties, Appl. Surf. Sci. Adv. 4 (2021), 100085, https://doi.org/10.1016/j.apsadv.2021.100085.
- [54] S. Nachimuthu, S. Thangavel, K. Kannan, V. Selvakumar, K. Muthusamy, M. R. Siddiqui, S.Mohammad Wabaidur, C. Parvathiraja, Lawsoniainermis mediated synthesis of ZnO/Fe<sub>2</sub>O<sub>3</sub> nanorods for photocatalysis Biological treatment for the enhanced effluent treatment, antibacterial and antioxidant activities, Chem. Phys. Lett. 804 (2022), 139907, https://doi.org/10.1016/j.cplett.2022.139907.
- [55] N. Suganth, S. Thangavel, K. Kannan, Hibiscus subdariffa leaf extract mediated 2-D fern-like ZnO/TiO<sub>2</sub> hierarchical nanoleaf for photocatalytic degradation, Flatchem 24 (2020), 100197, https://doi.org/10.1016/j.flatc.2020.100197.
- [56] H Mirzazadeh, M Lashanizadegan, Binary semiconductor oxide nanoparticles on graphene oxide (CdO/CeO<sub>2</sub>/RGO) for the treatment of hazardous organic water

- pollutants, Kor. J. Chem. Eng. 34 (2018) 1–10, https://doi.org/10.1007/s11814-017.02003
- [57] Y. Park, A. Numar, N. Ponomarev, J. Eqbal, M. Khalid, Enhanced photocatalytic performance of PANI-rGO-MnO<sub>2</sub> ternary composite for degradation of organic contaminants under visible light, J. Environ. Chem. Eng. 9 (2021), 106006, https://doi.org/10.1016/j.jece.2021.106006.
- [58] L. Fu, Y. Zheng, Z. Fu, W. Cai, J. Yu, Synthesis of Ag decorated graphenehierarchical TiO<sub>2</sub> nanocomposite with enhanced photocatalytic activity, Funct. Mater. Lett. 8 (2015), 1550036, https://doi.org/10.1142/S1793604715500368.
- [59] H. Mirzazadeh, M. Lashanizadegan, ZnO/CdO/reduced graphene oxide and its high catalytic performance towards degradation of the organic pollutants, J. Serb. Chem. Soc. 82 (2017) 1–16, https://doi.org/10.2298/JSC170630097M.
- [60] K. Sirohi, S. Kumar, V. Singh, N. Chauhan, A. Vohra, Synthesis, characterization and photocatalytic properties of graphene-CdO/SnO<sub>2</sub> ternary nanocomposites in visible light, Mater. Res. Express. 6 (2019), 075901, https://doi.org/10.1088/ 2053-1591/abl/22c
- [61] I.A. Alsafari, K. Chaudhary, M.F. Warsi, A. Warsi, M. Waqas, M. Hasan, A. Jamil, M. Shahid, A facile strategy to fabricate ternary WO<sub>3</sub>/CuO/rGO nano-composite for the enhanced photocatalytic degradation of multiple organic pollutants and antimicrobial activity, J. Alloy. Compnd. 938 (2023), 168537, https://doi.org/10.1016/j.jallcom.2022.168537.
- [62] R. Rakkappan, G.P. Halliah, Palladium-Decorated reduced graphene oxide/zinc oxide nanocomposite for enhanced antimicrobial, antioxidant and cytotoxicity activities, Process Biochem 93 (2020) 36–47, https://doi.org/10.1016/j. procbio.2020.03.010.
- [63] N. Belachew, M.H. Kahsay, A. Tadesse, K. Basavaiah, Green synthesis of reduced graphene oxide grafted Ag/ZnO for photocatalytic abatement of methylene blue and antibacterial activities, J. Environ. Chem. Eng. 8 (2020), 104106, https://doi. org/10.1016/j.jece.2020.104106.
- [64] S. Haq, M. Rashid, F. Menaa, N. Shahzad, M.I. Shahzad, S.Y.M. Alfaifi, O. Madkhali, M.D. Aljabri, M. Ashravi, R.A. Tayeb, M.M. Rahman, Antibacterial and antioxidant screening applications of reduced –graphene oxide modified ternary SnO<sub>2</sub>-NiO-CuO nanocomposites, Arab. J. Chem. 16 (2023), 104917, https://doi.org/10.1016/j.arabjc.2023.104917.
- [65] S. Shanavas, A. Priyadarsan, V. Vasanthakumar, A. Arunkumar, P.M. anbarasan, S. Bharathkumar, Mechanistic investigation of visible light driven novel La<sub>2</sub>CuO<sub>4</sub>/CeO<sub>2</sub>/rGO ternary hybrid nanocomposites for enhanced photocatalytic performance and antibacterial activity, J. Photochem. Photobiol A. Chem. 340 (2017) 96–108. https://doi.org/10.1016/j.iphotochem.2017.03.002.
- [66] V. Revathi, K. Karthik, Microwave assisted CdO-ZnO-MgO nanocomposite and its photocatalytic and antibacterial studies, J. Mater. Electron. 29 (2018) 18519–18530, https://doi.org/10.1007/s10854-018-9968-1.
- [67] K. Karthik, S. Dhanuskodi, C. Gopinath, S. Prabukumar, S. Sivaramakrishnan, Nanostructured CdO-NiO composite for multifunctional applications, J. Phys. Chem. Sol. 112 (2018) 106–118, https://doi.org/10.1016/j.jpcs.2017.09.016.
- [68] A.A. Ali Ahmed, Asma A.A. Al-Mushki, Bandar Ali Al-Ashahi, A.M. Abdulwahab, J. M.A. Abduljalil, F.A.A Saad, S.M.H. Qaid, H.M. Ghaithan, W.A. Farooq, A.H. Omar, Effect of ethylene glycol concentration on the structural and optical properties of multimetal oxide CdO-NiO-Fe<sub>2</sub>O<sub>3</sub> nanocomposites for antibacterial activity, J. Phys. Chem. Sol. 155 (2021), 110113, https://doi.org/10.1016/j.icoc.2021.10113.
- [69] K. Kannan, D. Radhika, R.D. Kasai, D. Gnanasangeetha, G. Palani, K. Gurushankar, R. Koutavarapu, D.Y. Lee, J. Shim, Facile fabrication of novel ceria-based nanocomposite (CYO-CSO) via co-precipitation: Electrochemical, photocatalytic and antibacterial performances, J. Mol. Struct. 1256 (2022), 132519, https://doi. org/10.1016/j.molstruc.2022.132519.
- [70] M. Suganya, A.R. Balu, D. Prabha, S. Anitha, S. Balamurugan, PbS-SnO<sub>2</sub> nanocomposite with enhanced magnetic, photocatalytic and antifungal properties, J. Mater. Sci. Mater. Electron. 29 (2018) 1065–1074, https://doi.org/10.1007/s10854-017-8007-v.
- [71] A. Jarosz, M. Skoda, I. Dudek, D. Szukiewicz, Oxidative stress and mitochondrial activation as the main mechanisms underlying graphene toxicity against human cancer cells, Oxidative Med. Cell. Longev. 2016 (2015), 5851035, https://doi.org/ 10.1155/2016/5851035.
- [72] Y. Liu, Y. Luo, J. Wu, Y. Wang, X. Yang, R. Yang, B. Wang, J. Yang, N. Zhang, Towards ultrahigh volumetric capacitance: graphene derived highly dense but porous carbons for supercapacitors, Sci. Rep. 3 (2013) 2975, https://doi.org/ 10.1038/srep02975.